Validation of a Smoothed Particle Hydrodynamics model for a highly aligned discontinuous fibre composites manufacturing process

S. Huntley[a], T. Rendall[a,*], M. Longana[a], T. Pozegic[a], K. Potter[a], I. Hamerton[a]

[a]*Bristol Composites Institute (ACCIS), Department of Aerospace Engineering, School of Civil, Aerospace, and Mechanical Engineering, Queen's Building, University Walk, Bristol, BS8 1TR, United Kingdom*

Abstract

This work presents a computational model for a discontinuous fibre composite manufacturing process. The alignment mechanism of this novel process, called the High Performance Discontinuous Fibre (HiPerDiF) method, involves highly coupled fluid-structure interactions. Fibres with a length on the order of a few millimetres are placed in a water suspension, sprayed between two parallel plates and deposited on a moving belt to make an aligned discontinuous fibre tape. This technology can be used as part of a composites recycling process to remanufacture reclaimed fibres into valuable recycled composite feedstock by ensuring a high level of alignment. In order to industrialise this process, the throughput must be increased whilst maintaining the high level of alignment. This work aims to assist this development by modelling the alignment mechanism using smoothed particle hydrodynamics (SPH). It is shown through comparison to experiments that SPH models the process well and captures the influences affecting fibre alignment.

Keywords: Recycling, Aligned discontinuous fibres, Smoothed Particle Hydrodynamics
2010 MSC: 00-01, 99-00

*Corresponding author
Email address: thomas.rendall@bristol.ac.uk (T. Rendall)

1. Introduction

Carbon fibre reinforced polymer composites (CFRPs) continue to become increasingly important; their use has been steadily growing over the past few decades in a wide range of industries. They have acheived this status due to their nature as high quality products that exhibit high strength and stiffness, low density and fatigue and corrosion resistance. The use of virgin carbon fibre is expensive and with increasing amounts being produced represents a significant environmental challenge with regards to manufacturing and end of life waste disposal.

This has led to a growing interest in developing methods that allow composite waste to be recycled. Excluding mechanical grinding that generates low value materials, composite recycling is a two step process: the degradation of the matrix to reclaim the fibres and their remanufacturing in a new recycled material [1]. Independently of the matrix degradation processes, that might be based on pyrolytic or solvolytic processes, the reclaimed fibres are in a filamentised, random, low-density-packing (fluffy) form [2]. To obtain a high-performance, and therefore valuable, recycled composite material it is of paramount importance that the fibres are realigned to obtain high fibre volume fraction [3]. One process that has been invented at the University of Bristol that enables the production of highly aligned, discontinuous composites is the High Performance Discontinuous Fibre (HiPerDiF) method [4, 5, 6, 7]. Explained in more detail below, the primary aligment mechanism is through the suspension of the fibres, with length between 1 and 12 mm, in a water jet, which is sprayed between thinly spaced parallel plates. In order to industrialise this process, the main improvement needed is an increase in the throughput. However, this needs to be achieved whilst maintaining the excellent alignment level. To facilitate this the fluid mechanics behind the alignment process must be better understood.

The aim of this work is to develop a computational model to investigate this highly coupled fluid structure interation problem and this will be achieved using smoothed particle hydrodynamics (SPH). SPH has been chosen due to its excellent ability to model both free-surface flows and cases with large amounts of deformation, as will be the case in this project. SPH is a meshless, Lagrangian method originally developed by both Lucy [8] and Gingold and Monaghan [9] for astrophysics problems. It is a relatively new method compared to standard mesh based computational fluid dynamics methods. One of the main areas of development has been on breaking waves

but it has also been widely applied to impact and explosion problems, multiphase flows and heat and mass transfer problems, demonstrating its excellent versatility. There are also examples in the literature of authors using SPH to model flows that contain short fibres. One of the first examples was to model the flow of self-compacting concrete with steel fibres by Kulasegaram and Karihaloo [10], which was further developed by Deeb *et al.* [11]. They used incompressible SPH to model the non-Newtonian fluid and rigid body fibres. SPH has also been used to model the injection molding process for composites manufacturing by He *et al.* [12], whilst Wu *et al.* [12] used a coupled SPH-DEM approach whereby the fibres were modelled as discrete element method (DEM) particles. Whilst these applications share some similarities with this work in terms of the suspension of short fibres in a medium, the flows investigated were all more viscous than the fluid used in this work.

The primary focus of this work is the final fibre orientation and alignment as this is crucial for producing material that has comparative mechanical properties to traditional continuous fibre components. Investigations into fibre orientation have been explored for several different flow types using a variety of methods. Fibre orientation has been studied using SPH by Skoptsov *et al.* [13] for the injection molding process and was also the focus of the investigation of Deeb *et al.* [14] for self-compacting concrete. Other studies of fibre orientation using different methods include Oumer *et al.* [15], who looked at fibre orientation of injection molding using the software MoldFlow and Khodadadi Yazdi *et al.* [16] who used a finite volume approach to study the flow of short fibres through a planar contraction. However, most relevant for this work is perhaps the study by Hamalainen *et al.* [17] who discussed the fibre alignment of a paper-making process, which has a similar setup to the HiPerDiF process, using an Eulerian based approach.

As previously stated, the HiPerDiF alignment mechanism is a highly coupled fluid-structure interaction problem between the water and the fibres. Here both the fluid and fibres are modelled using SPH particles and the fibres are treated as rigid bodies. An example of an SPH simulation in two dimensions is given in Fig. 1. This is a technique also used by other authors such as Hashemi *et al.* [18] and Tofighi *et al.* [19] whose work focused on moving particles in a fluid or named particle suspensions and used weakly compressible and incompressible SPH, respectively. Also, Aly and Asai [20] used the same technique to simulate flood disaster using incompressible SPH.

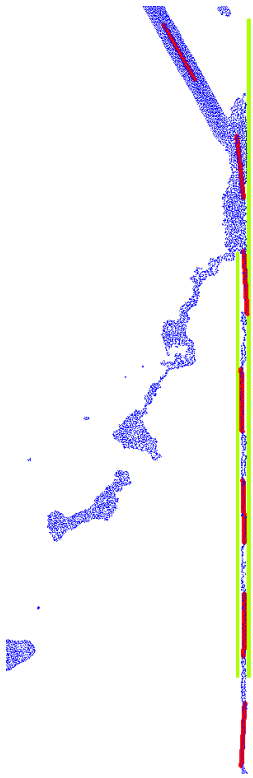

Figure 1: Example of SPH simulation in 2D. Blue are fluid particles, green are wall particles and red are fibre particles

1.1. The HiPerDiF method

The High Performance Discontinuous Fibre (HiPerDiF) method is a manufacturing process invented at the University of Bristol to produce highly aligned discontinuous fibre tapes. A schematic of the HiPerDiF technology is shown in Fig. 2.

The process begins with a low concentration of fibres in a water suspension tank. Fibres are then sprayed through a nozzle towards an array of thinly-spaced parallel plates, known as the alignment head. The momentum change induced by this action causes the fibres to align. After this, they drop onto a moving mesh conveyer belt. This perforated belt allows the water to be extracted without affecting the fibre alignment, which is aided by the use of a suction pump. This leaves the aligned fibres on the belt, before being fully dried and impregnated with the resin. The alignment of the fibres is crucial to producing commercially valuable material. As such, it is important to

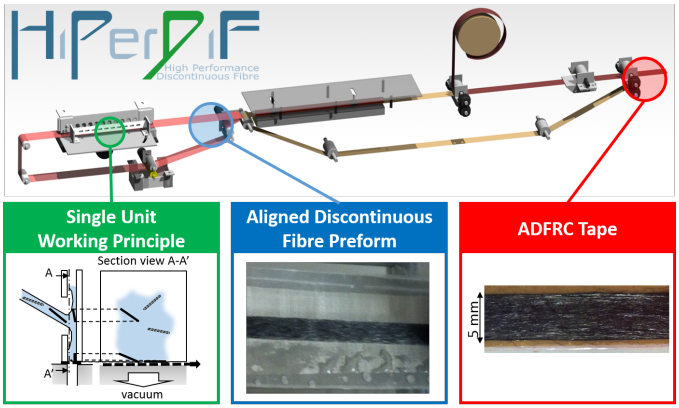

Figure 2: HiPerDiF composite manufacturing process

investigate the physics behind the problem in order to better understand the factors influencing the fibre alignment.

This paper presents the SPH model of the HiPerDiF alignment mechanism and the validation against experimental results. The remainder of this paper is ordered as follows: section 2 outlines the methodology used in the SPH simulations of the HiPerDiF alignment process and section 3 presents the validation results of the SPH model by comparing the simulation to equivalent experimental setups.

2. Smoothed Particle Hydrodynamics

SPH is a meshless Lagrangian method. The most common way of formulating the SPH equations involves discretising the domain into a set of particles, which represent interpolation points. A function, $F(\mathbf{r}_i)$, can then be computed as a sum over neighbouring particles using

$$F(\mathbf{r}_i) = \sum_j \frac{m_j}{\rho_j} F(\mathbf{r}_j) W(\mathbf{r}_i - \mathbf{r}_j, h) \tag{1}$$

where W is the a smoothing kernel function, m_j, ρ_j and $\mathbf{r}_j$ are the mass, density and position of particle j, respectively and h is the smoothing length, which is typically set to be larger than the initial particle spacing, Δs, ie $h = 1.5\Delta s$. Then the sum is performed over all neighbouring particles within a certain radius which is dependent on the kernel used but for this work the

radius is $2h$ or $3\Delta s$. A large number of different smoothing kernels have been used in the literature. In this work, Wendland's C2 function is used:

$$W(\mathbf{r}_i - \mathbf{r}_j, h) = \begin{cases} \alpha \left(1 - \frac{q}{2}\right)^4 + (2q+1), & 0 \leq q \leq 2 \\ 0, & \text{otherwise} \end{cases} \tag{2}$$

where $q = |\mathbf{r}_i - \mathbf{r}_j| / h$ and $\alpha = 21/16\pi h^3$ for three dimensions. This formulation can also be used to construct the gradient of $F(\mathbf{r}_i)$, which is given by

$$\nabla F(\mathbf{r}_i) = \sum_j \frac{m_j}{\rho_j} F(\mathbf{r}_j) \nabla W(\mathbf{r}_i - \mathbf{r}_j, h) \tag{3}$$

The equations governing the particles are the continuity and Navier-Stokes equations, which are given by

$$\frac{d\rho}{dt} = -\rho \nabla \cdot \mathbf{v} \tag{4}$$

$$\frac{d\mathbf{v}}{dt} = -\frac{\nabla p}{\rho} + \frac{\nu}{\rho} \nabla^2 \mathbf{v} + \mathbf{g} \tag{5}$$

where $\mathbf{v}$ is the velocity, t is time, p is pressure, ν is viscosity and $\mathbf{g}$ is gravity.

In this work, the weakly compressible form of SPH is used. This gives the discretised continuity equation as

$$\frac{d\rho_i}{dt} = \sum_j m_j (\mathbf{v}_i - \mathbf{v}_j) \cdot \nabla W(\mathbf{r}_i - \mathbf{r}_j, h) \tag{6}$$

The right hand side of Eq. (6) is an approximation to $\mathbf{v} \cdot \nabla \rho$ because $\nabla \cdot \mathbf{v} = 0$ as this is incompressible. The momentum equation, Eq. (5), can be discretised as

$$\begin{aligned} \frac{d\mathbf{v}_i}{dt} &= -\sum_j m_j \left[\frac{p_j}{\rho_j^2} + \frac{p_i}{\rho_i^2}\right] \nabla W(\mathbf{r}_i - \mathbf{r}_j, h) \\ &+ \sum_j m_j \nu \frac{\rho_i + \rho_j}{\rho_i \rho_j} \frac{(\mathbf{r}_i - \mathbf{r}_j) \cdot \nabla W(\mathbf{r}_i - \mathbf{r}_j, h)}{|\mathbf{r}_i - \mathbf{r}_j|^2 + 0.001h^2} \mathbf{v}_{ij} \\ &+ \frac{1}{m_i} \mathbf{F}_i + \mathbf{g} \end{aligned} \tag{7}$$

The first term on the right hand side of Eq. (7) is a symmetrical, balanced form of the pressure term, an approximation to $\frac{\nabla p}{\rho}$ which could also

be approximated in other ways as described by Price [21]. The second term is the viscosity term proposed by Morris *et al.* [22] and the third term is pairwise force surface tension described by Tartakovsky and Meakin [23].

In order to complete the formulation, an equation of state is required to compute the pressures. In this work, the Murnaghan-Tait equation of state, Eq. (8), is used.

$$p = B\left[\left(\frac{\rho}{\rho_0}\right)^{\gamma} - 1\right] \tag{8}$$

The value of γ is set to 7 as originally suggested by Cole [24]. The value of B is given by $B = c_0^2\rho_0/\gamma$, where c_0 is the speed of sound and is set to a value an order of magnitude greater than the largest velocity expected in the simulation as proposed by Monaghan [25]. This is done to keep the density fluctuations small.

After formulating the discretised equations for the particles, the problem is integrated in time using the Newmark-beta method as explained by Hall *et al.* [26].

2.1. Boundary particles

There are several options available to model solid boundaries in SPH. These vary in complexity and accuracy; a good summary is provided by Fraga Filho and Chacaltana [27]. In this work, the solid boundaries are modelled using dynamic boundary particles as originally proposed by Dalrymple and Rogers [28] and later developed by Crespo *et al.* [29]. These are SPH particles that are fixed, for wall particles, or moving with a prescribed motion, for belt particles. Essentially only the continuity equation, Eq. (6), is solved for these particles.

2.2. Modelling the fibres

The fibres are also modelled using SPH particles. However, the particles making up a fibre are constrained by rigid body kinematics. So after solving the momentum and continuity equation for the fibre particles, the linear and angular velocities, V and Ω respectively, of each fibre are updated using Eq. (9) and Eq. (10)

$$M\frac{dV}{dt} = F \tag{9}$$

$$I\frac{d\Omega}{dt} = T \tag{10}$$

where M is the mass of the fibre, F is the total force on the fibre computed by summing the contribution from the particles that belong to it, I is the inertia matrix and T is the torque. The fibres are modelled as thin rods meaning that there is no rotation about length. The velocities computed using these equations can then be used to update the positions of all of the particles on a given fibre.

2.3. Fluid-Structure coupling

In this application, the fluid and structure represents a highly coupled system. Therefore, it is necessary to ensure that a strongly coupled fluid-structure algorithm is used. The strongly coupled procedure used in this work is presented in Fig. 3.

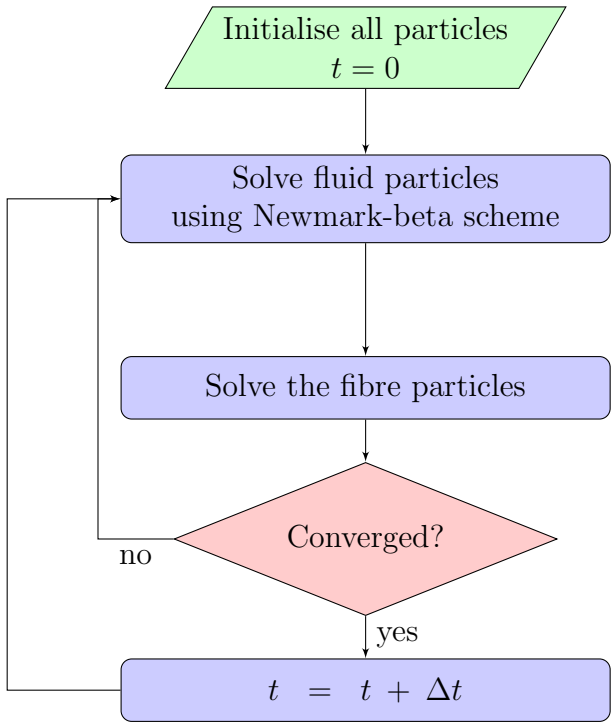

Figure 3: Flowchart of the coupled fluid-structure interaction

One iteration of the algorithm consists of computing the new positions and velocities of the fluid particles and the new densities and pressures of all the particles. Then, using the latest values for the fluid variables, new

positions and velocities of the fibre particles are calculated. If the positions are converged, then a new time step is initiated. If not, the fluid variables are reset and the latest fibre position and velocities are used to recalculate the fluid values. This is repeated until convergence is achieved. Typically, in this application, 2 or 3 iterations are needed for convergence. This results in a process that is fully implicit, which is important as there is a strong coupling between the fluid and the fibres.

The aim of this work is to validate the general SPH approach to modelling the HiPerDiF alignment head and as shown in the next section, the model accuracy and stability is appropriate for this problem.

3. Results

This work provides validation of the SPH model used to simulate the HiPerDiF alignment process. First the experimental setup is presented and then the computational setup is described. Finally, the results from both are compared and show that the SPH model accurately represents the alignment mechanism.

3.1. Experimental setup

The experiments used a smaller prototype version of the HiPerDiF machine. The working principles are the same but the alignment head consists of two nozzles as shown in Fig. 4. The validation was carried out by comparing the effect of different plate spacings on the fibre alignment. Three different plate spacings were used: 0.3 mm, 0.5 mm, and 1.0 mm. All other settings remained constant and are listed in Table 1.

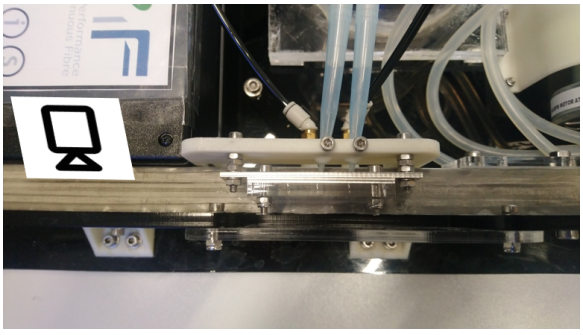

Figure 4: Smaller prototype HiPerDiF alignment head. The camera shows the angle at which the fibres were captured in Fig. 9, which is from directly above the belt.

Table 1: Experimental parameters

Parameter name	Value	Units
Nozzle angle θ	45.0	degrees
Nozzle angle ϕ	45.0	degrees
Nozzle diameter	1.35	mm
Flow rate	2.35	mL/s
Belt speed	14	mm/s
Fibre length	3.0	mm
Fibre density	1820	kg/m^3
Fibre volume concentration	0.0005	%

3.2. Computational setup

The computational setup, showwn in Fig. 5, was designed to closely match the experiments. Most parameters are straightforward to implement such as the nozzle angles, belt speed and fibre properties. However, as the machine uses a peristaltic pump, this has the effect of pulsing the jet. Therefore, it was necessary to include this effect in the simulations. The pulse was timed at 0.025 seconds on and 0.025 seconds off. This was modelled by a clipped sinusoidal function, shown in Fig. 6, so that the overall flow rate matched the value calculated in the experiments. Also, the fibre concentration was used to calculate the number of fibres assuming that the fibres are evenly dispersed in the water and evenly supplied to the nozzles. This resulted in 4 fibres per nozzle per pulse.

For all three plate spacings, the particle smoothing length was kept constant. The resolution requirements are primarily driven by the plate spacing due to the need to accurately resolve the gap. It is important to resolve the gap but not to over-resolve it as this unnecessarily increases the computational cost. Therefore, the smallest plate spacing was used to determine the smoothing length, which was set to 0.09 mm, which is 1.5 times the initial particle spacing. This initial particle spacing was determined from a resolution study where the simulation was performed with progressively smaller initial particle spacing and the final alignment quantified, shown in Fig. 7. All the simulation parameters are provided in Table 2.

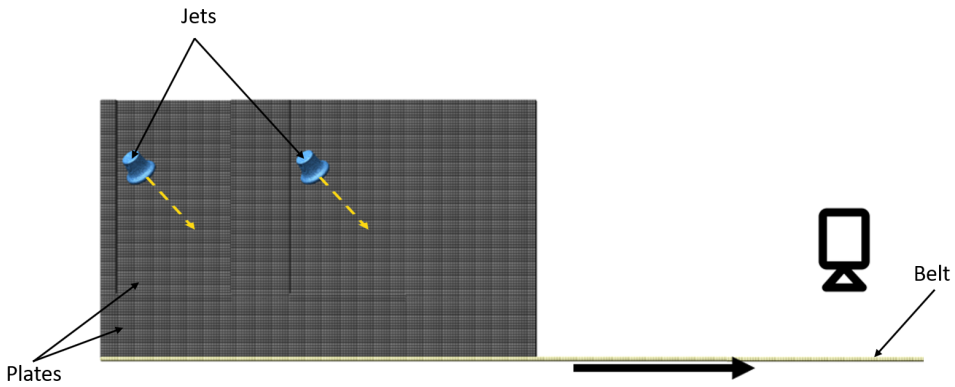

Figure 5: Side-on view of the simulation setup of the smaller protoype alignment head. The thick arrow indicates the belt direction and the dashed arrows indicate direction of the jets. The camera shows the angle at which the images were captured in Fig. 9.

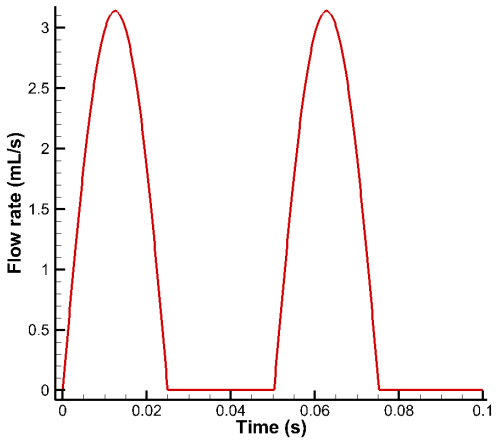

Figure 6: Jet pulse function

3.3. Validation results

The results presented here form the basis for the validation of the SPH model of the HiPerDiF alignment mechanism. This was performed in two ways. The first is a comparison of the shape of the jet impingement on the plate and the second is a comparison of the relative fibre alignment as the plate spacing is altered.

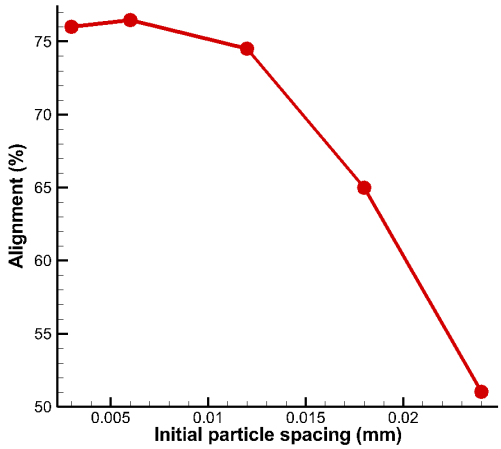

Figure 7: Fibre alignment with different initial particle spacing for a plate width of 0.3 mm.

3.3.1. Jet formation

The formation of the jet as it impinges the back plate was captured using a high speed imaging camera. The camera was a Photron FASTCAM SA-Z and took images at 20000 frames per second. The images were taken from behind the plate. Fig. 8 shows the shape the jet forms on the plate at different instances of the pulsing action. Comparison of the experimental jet, Fig. 8(a), and the computational jet, Fig. 8(b), shows the simulations match the experimental reality well.

Table 2: Computational parameters

Parameter name	Value	Units
Initial particle spacing	0.06	mm
Surface tension coefficient	0.0728	N/m
Smoothing length	0.09	mm
Contact angle (plates)	71.0	degrees
Contact angle (fibres)	80.0	degrees
Timestep size	2×10^{-7}	seconds
FSI loop iterations	2	n/a

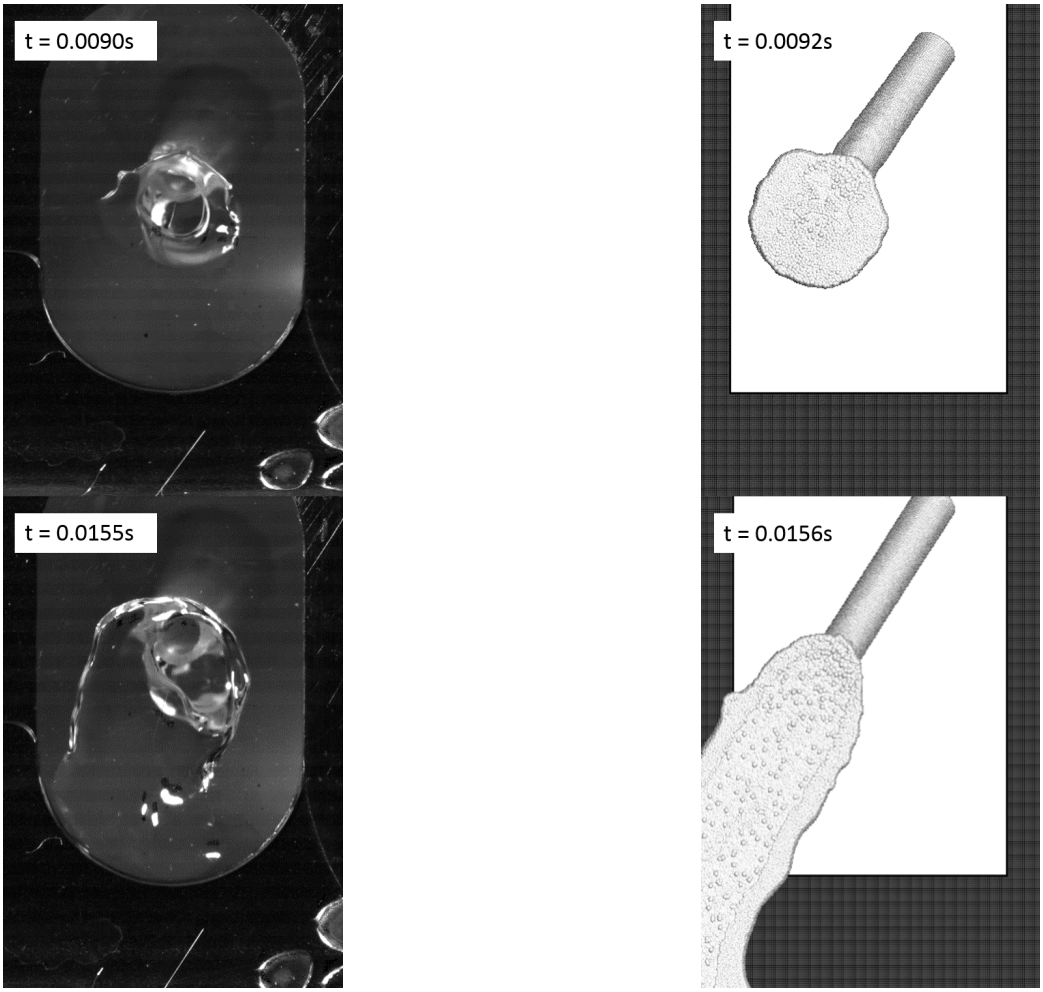

(a) Experimental jet (b) Computational jet

Figure 8: Shape formed by jet impinging on the plate

3.3.2. Fibre alignment

For each plate spacing, the preform produced was carefully transferred to a glass slide and imaged. The images were taken from the angle indicated by the camera symbol in Figs. 4 and 5 for the experimental and computational results respectively. The fibre alignment for the three different plate spacings is shown in Fig. 9. It is clear that the experimental alignment, Fig. 9(a), decreases as the plate spacing increases and this trend is captured by the SPH model, Fig. 9(b). One of the benefits of having a computational model

is that the fibre alignment can be easily quantified. This has been done for the three plate spacings and is shown in Fig. 10, which shows the percentage of fibres aligned within ±3° of the belt direction. This figure quantifies the decrease in fibre alignment as the plate spacing is increased, with the smallest plate spacing having an alignment of 76% reducing to 27% for the largest plate spacing. The alignment from the experimental fibres can also be quantified using software such as OrientationJ [30]. Developed in the field of biomedical engineering, OrientationJ uses directional image analysis to characterise the orientation properties in an image based on evaluation of the gradient structure tensor in a local neighborhood. Performing this analysis on the images in Fig. 9(a) produces a distribution plot as shown in Fig. 11 for the 0.5 mm plate spacing. This is used to calculate the percentage of fibres within ±3° and the results are shown in Fig. 10.

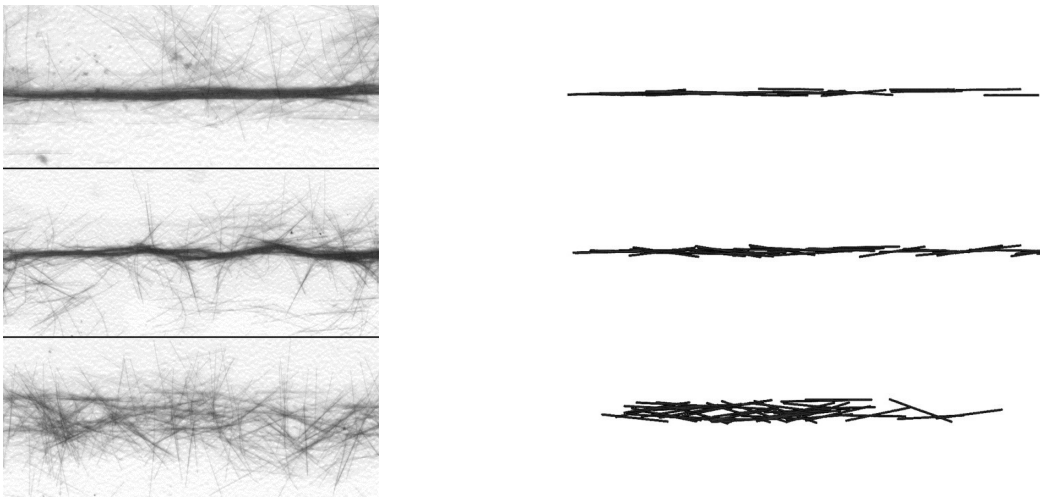

(a) Experimental fibre alignment

(b) Computational fibre alignment

Figure 9: Fibre alignment for different plate spacings

Although it may appear that some of the fibres have deformed in Fig. 9(a) the authors have found this to be an optical illusion caused by the large number of small, thin fibres that makes it extremely difficult to distinguish individual fibres in this figure. As such, it is probable that where a fibre appears to have deformed this is probably a number of fibres that overlay in such away that they give the appearance of a single deformed fibre. This is supported by magnified views of the fibres shown in Fig. 12, which are

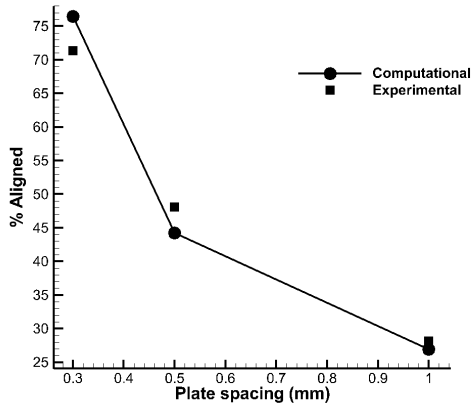

Figure 10: Effect of plate spacing on fibre alignment

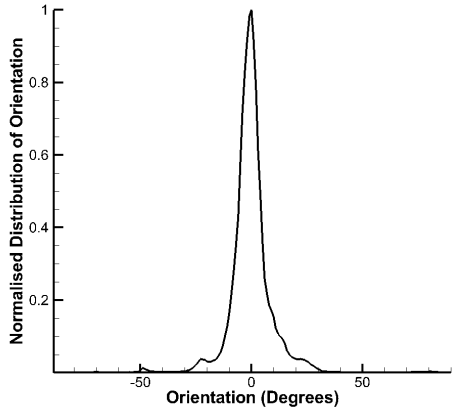

Figure 11: Dsitribution plot of fibre orientation of 0.5 mm plate spacing produced by OrientationJ.

representative of the entire preform of fibres. The rigid body assumption is also supported by bending beam calculations performed by the authors. The fibres were modelled as a thin beam in crossflow. Calculating the drag on a fibre from the maximum velocity, and asscosited drag coefficient as given by Lindsey [31], using equation (11), resulted in a maximum deflection of 0.20 mm for 3 mm long fibres, in other words 6.6% of its length. A reasonable assumption for rigid bodies is a deformation no greater than 10% of the length

therefore; modelling these fibres as rigid bodies is valid in this instance.

$$D = \frac{1}{2}\rho V^2 S C_D \tag{11}$$

This calculation can also be used to compute the maximum length of fibres for this jet velocity or conversely the maximum jet velocity for this length of fibres where this assumption still holds. For example, for this jet velocity the longest fibres where this assumption holds is 3.5 mm and the maximum jet velocity for 3 mm fibres is 2.45 m/s. This is, however, a conservative calculation as the the fibre slip velocity is less than the jet velocity, which has been used in this calculation.

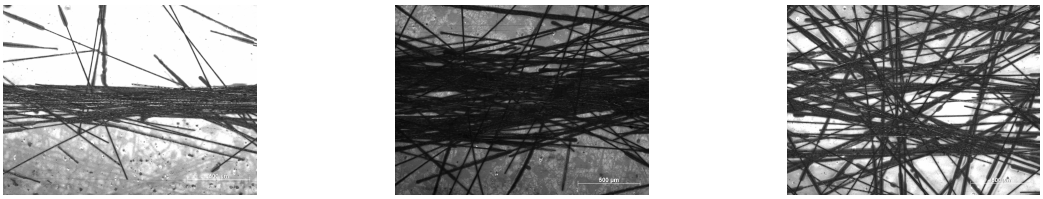

(a) 0.3 mm plate spacing

(b) 0.5 mm plate spacing

(c) 1.0 mm plate spacing

Figure 12: Magnified view of fibres in Fig. 9.

3.4. Effect of jet velocity

Having validated the model, the effect of the jet velocity on the fibre alignment was investigated. For these simulations the pulsing effect of the jet was ignored, instead a continuous flow was modelled for four different velocities: 0.4 m/s, 0.8 m/s, 1.6 m/s, and 3.2 m/s. These jet velocities were investigated for two different plate spacings: 0.3 mm and 1.0 mm. A continuous jet with velocity 0.8 m/s displaces the same amount of fluid in 0.05 seconds as the pulsing jet simulated previously. The number of fibres introduced was constant with respect to time for all velocities, thus meaning that the faster jets had a lower fibre concentration than the slower ones. The fibre alignment for the four different jet velocities are shown in Fig. 13 and Fig. 14 for a plate spacing of 0.3 mm and 1.0 mm, respectively. It is clear to see that the level of alignment is largely unaffected by the jet velocity. For the smaller plate spacing there is very little difference between any of the simulations. For the largest plate spacing, the effect of increasing jet velocity

is to stretch the placement of fibres out in the belt direction, which results in both a thinner tape and one that would contain more voids, thus having lower quality. As mentioned in the previous section the assumption of the fibres acting as rigid bodies is potentially not valid for the jet velocity of 3.2 m/s.

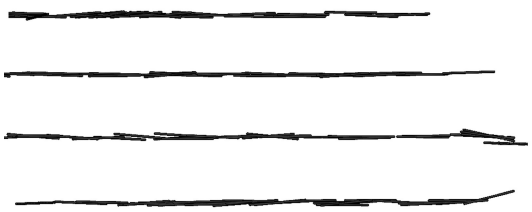

Figure 13: Fibre alignment for plate spacings of 0.3 mm for jet velocities of 0.4 m/s, 0.8 m/s, 1.6 m/s, 3.2 m/s (top to bottom)

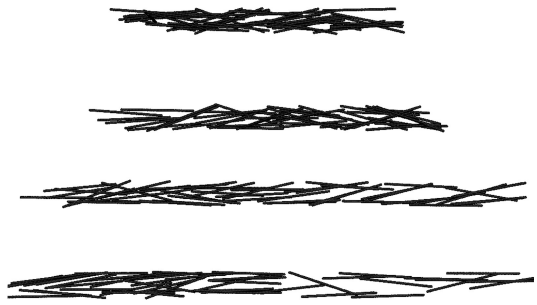

Figure 14: Fibre alignment for plate spacings of 1.0 mm for jet velocities of 0.4 m/s, 0.8 m/s, 1.6 m/s, 3.2 m/s (top to bottom)

3.5. Characterisation of flow rate for production

The SPH simulations can also be used to determine a relationship between mass flow rate between the plates and jet velocity. In combination with the input parameters it is possible to determine a characteristic, non-dimensional curve for a given geometry. In two dimensions, this means for a given nozzle diameter, d, plate spacing, l, hydrostatic head, h and nozzle angle, θ, (as shown in Fig. 15) the relationship between the discharge coefficient and the

jet coefficient can be computed. This discharge coefficient is given by

$$C_{dis} = \frac{V_d}{\sqrt{2gh}} \tag{12}$$

where V_d is the discharge velocity and g is gravity and the jet coefficient is given by

$$C_{jet} = \frac{V_j}{\sqrt{2gh}} \tag{13}$$

where V_j is the jet velocity. The mass flow rate is calculated by recording the mass flow between the plates over the course of the simulation and is used to determine the discharge velocity using $\dot{m} = \rho l V_d$. A representative time history of mass flow is shown in Fig. 16. The mass flow rate can then be computed by calculating the gradient of the curve once the initial transient has settled to a steady state. This relationship was calculated for several

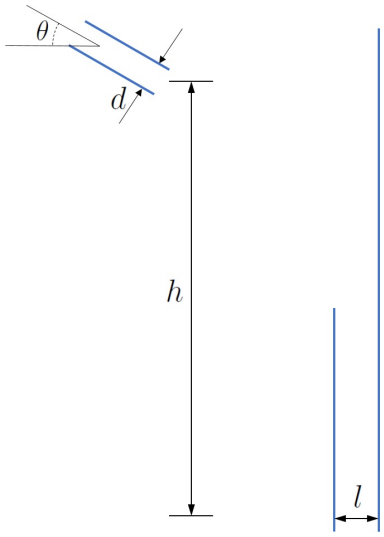

Figure 15: Two-dimensional geometry used to determine characteristic curves

nozzle angles and two different plate spacings: one where the nozzle diameter was approximately the same as the plate spacing and one where the nozzle diameter was much larger than the plate spacing. The simulations were also run once keeping the Reynolds number constant (by changing the viscosity) as typically done for these curves and once allowing the Reynolds number to vary as is the reality when using the same fluid. The results can be

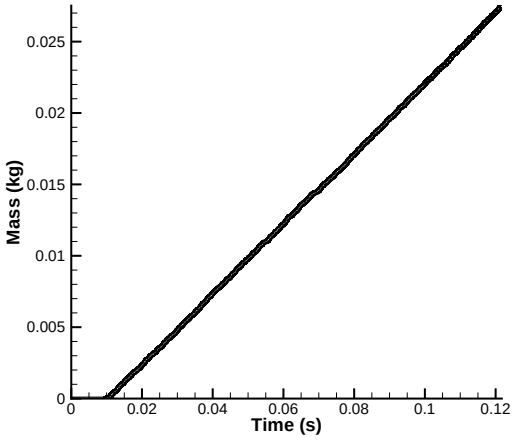

Figure 16: Example of the mass flow rate

seen in Fig. 17. From these graphs it can be seen that for a nozzle with a similar diameter to the plate spacing with a constant Reynolds number, Fig. 17(a), the effect of increasing the nozzle angle is to increase the discharge coefficient for increasing jet coefficient. This is because the viscosity increases to allow the Reynolds number to remain the same meaning that there is less splash and therefore a higher flow rate between the plates. By allowing the Reynolds number to vary, Fig. 17(b), this effect is removed and therefore there is a convergence of the relationship between discharge coefficient and jet coefficient at the higher nozzle angles with the exception of the case when the nozzle angle is 90 degrees and is thus directed precisely between the plates. This effect due to viscosity is highlighted in Fig. 18, which shows a snapshot of the particle positions for a nozzle angle of 75° and a jet coefficient of 6, where it can be seen that the the case with a varying Reynolds number, and therefore a lower viscosity, (Fig. 18(b)) deflects off the wall more than the case with a constant Reynolds number and thus higher viscosity (Fig. 18(a)). It can also be seen that for the larger nozzles, Figs. 17(c) and 17(d), the influence of the nozzle angle has been removed such that the relationship between discharge coefficient and jet coefficient is independent of the nozzle angle. This is a result of the nozzle being much larger than the plate spacing such that the gap between the plates is saturated at all times. This effect of saturation is shown in Fig. 19, which shows a snapshot of the particle

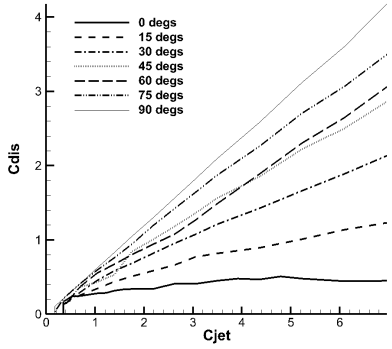

(a) Small nozzle with constant Reynolds number

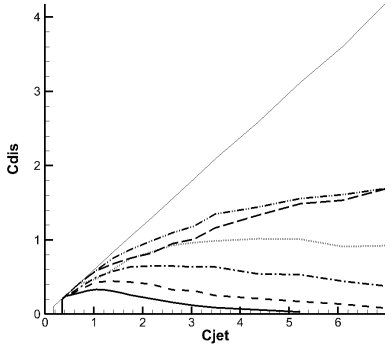

(b) Small nozzle with varying Reynolds number

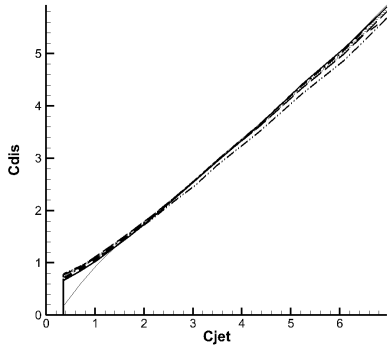

(c) Large nozzle with constant Reynolds number

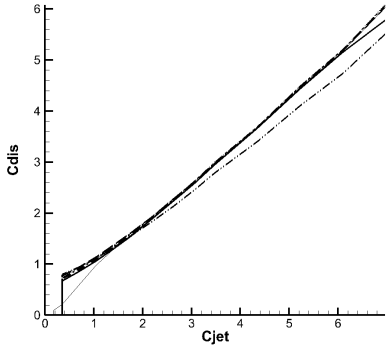

(d) Large nozzle with varying Reynolds number

Figure 17: Discharge coefficient against jet coefficient for different nozzle angles

positions for the large nozzle (Fig. 19(a)) and small nozzle (Fig. 19(b)) for a nozzle angle of 15° and a jet coefficient of 3 for a constant Reynolds number. It can be seen that the large nozzle completely saturates the gap between the plates but also there is a lot more water that misses the gap. As the current HiPerDiF setup employs a nozzle that has a diameter much larger than the plate spacing these results suggest that currently any nozzle angle could be employed to maintain the same discharge coefficient. However, it also suggests that there is a significant amount of excess water being used and from a purely hydrodynamic perspective (ignoring any effects from the

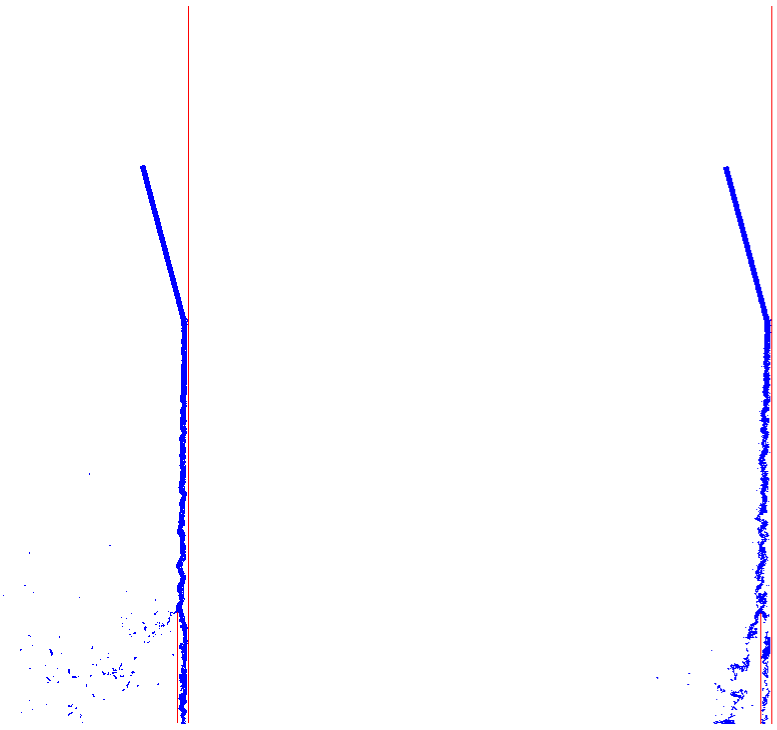

(a) Constant Reynolds number (b) Varying Reynolds number

Figure 18: Particle positions for small nozzle with an angle of 75° and jet coefficient of 6

fibres) a smaller nozzle could be used.

4. Conclusion

A numerical fluid model for deposition of suspended fibres has been presented based on smoothed particle hydrodynamics. The model includes all fluid-fibre effects, as well as the influence of the peristaltic pump, pressure-driven fluid drainage and moving belt. Accuracy has been assessed against experimental results by varying the plate spacing of the tape laying machine, and the numerical model has been shown to correctly reproduce the variations

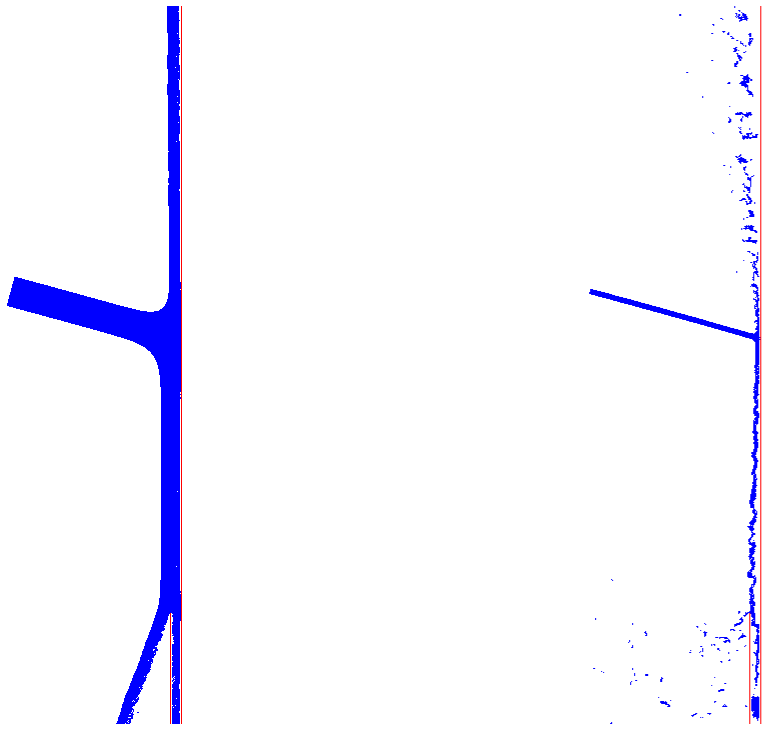

(a) Large nozzle (b) Small nozzle

Figure 19: Particle positions for different nozzle sizes with an angle of 15° and jet coefficient of 3 with a constant Reynolds number

in fibre alignment observed. This SPH approach to fluid-fibre interaction has the potential to be further extended and be useful in understanding other composite manufacturing processes such as injection moulding and extrusion. Future work will focus on higher fidelity modelling of the system as the HiPerDif machine design progresses and investigation of the wide range of parameters that could potentially affect the alignment.

Acknowledgements

This research was funded by the UK Engineering and Physical Sciences Research Council (EPSRC) "High Performance Discontinuous Fibre Composites - A sustainable route to the next generation of composites" [EP/P027393/1] grant.

References

[1] G. Oliveux, L. Dandy, G. Leeke, Current status of recycling of fibre reinforced polymers: Review of technologies, reuse and resulting properties, Progress in Materials Science 72 (2015) 61–99. doi:j.pmatsci.2015.01.004.

[2] S. Pimenta, S. Pinho, Recycling carbon fibre reinforced polymers for structural applications: Technology review and market outlook, Waste Management 31 (2) (2011) 378–392. doi:j.wasman.2010.09.019.

[3] M. Longana, N. Ong, H. Yu, K. Potter, Multiple closed loop recycling of carbon fibre composites with the hiperdif (high performance discontinuous fibre) method, Composite Structures 153 (2016) 271–277. doi:http://dx.doi.org/10.1016/j.compstruct.2016.06.018.

[4] M. Longana, H. Yu, M. Jalavand, M. Wisnom, K. Potter, Aligned discontinuous intermingled reclaimed/virgin carbon fibre composites for high performance and pseudo-ductile behaviour in interlaminated carbon-glass hybrids, Journal of Composites Science and Technology 143 (2017) 13–21. doi:10.1016/j.compscitech.2017.02.028.

[5] M. Longana, H. Yu, I. Hamerton, K. Potter, Development and application of a quality control and property assurance method for reclaimed carbon fibers based on the hiperdif (high performance discontinuous fibre) method and interlaminated hybrid specimens, Advanced Manufacturing: Polymer and Composites Science 4 (2) (2018) 48–55. doi:10.1080/20550340.2018.1456504.

[6] R. Tapper, M. Longana, H. Yu, I. Hamerton, K. Potter, Development of a closed-loop recycling process for discontinuous carbon fibre polypropylene composites, Composites Part B: Engineering 146 (2018) 222–231. doi:10.1016/j.compositesb.2018.03.048.

[7] R. Tapper, M. Longana, I. Hamerton, K. Potter, A closed-loop recycling process for discontinuous carbon fibre polyamide 6 composites, Composites Part B: Engineering 179. doi:10.1016/j.compositesb.2019.107418.

[8] L. Lucy, A numerical approach to the test of the fission hypothesis, The Astronomical Journal 82 (12) (1977) 1013–1024.

[9] A. Gingold, J. Monaghan, Smoothed particle hydrodynamics: Theory and application to non-spherical stars, Monthly notices of the Royal Astronomical Socitey 181 (375–389).

[10] S. Kulasegaram, B. Karihaloo, A. Ghanbari, Modelling the flow of self-compacting concrete, International Journal for Numerical and Analytical Methods in Geomechanics 35 (2011) 713–723. doi:10.1002/nag.924.

[11] R. Deeb, S. Kulasegaram, B. Karihaloo, 3d modelling of the flow of self-compacting concrete with or without steel fibres. part i: slump flow test, Computational Particle Mechanics 1 (2014) 373–389. doi:10.1007/s40571-014-0002-y.

[12] L. He, G. Lu, D. Chen, W. Li, C. Lu, Three-dimensional smoothed particle hydrodynamics simulation for injection molding of short fiber-reinforced polymer composites, Modelling and Simulation in Materials Science and Engineering 25 (055007). doi:10.1088/1361-651X/aa6dc9.

[13] K. Skoptsov, V. Sheshenin, V. Galatenko, A. Malakho, N. Shornikova, V. Avdeev, V. Sadovnichy, Particle simulation for predicting effective properties of short fiber reinforced composites, International Journal of Applied Mechanics 8 (1650016). doi:10.1142/S1758825116500162.

[14] R. Deeb, S. Kulasegaram, B. Karihaloo, 3d modelling of the flow of self-compacting concrete with or without steel fibres. part ii: L-box test and the assessment of fibre reorientation during the flow., Computational Particle Mechanics 1 (2014) 391–408. doi:10.1007/s40571-014-0003-x.

[15] A. Oumer, N. Hamidi, I. Mat Sahat, Numerical prediction of flow induced fibers orientation in injection molded polymer composites, in:

IOP Conf. Series: Materials Science and Engineering, Vol. 100, IOP Publishing Ltd, 2015. doi:10.1088/1757-899X/100/1/012066.

[16] M. Khodadadi Yazdi, A. Ramazani S.A., A. Kamyabi, H. Hosseini Amoli, Simulation of flow of short fiber suspensions through a planar contraction, Transactions C: Chemistry and Chemical Engineering 19 (2012) 579–584. doi:10.1016/j.scient.2012.04.008.

[17] J. Hamalainen, T. Hamalainen, T. Leppanen, H. Niskanen, J. Sorvari, Mathematics in paper - from fiber suspension fluid dynamic to solid state paper mechanics, Journal of Mathematics in Industry 4 (14). doi:10.1186/2190-5983-4-14.

[18] M. Hashemi, R. Fatehi, M. Manzari, A modified sph method for simulating motion of rigid bodies in newtonian fluid flows, International Journal of Non-Linear Mechanics 47 (2012) 626–638. doi:10.1016/j.ijnonlinmec.2011.10.007.

[19] T. Tofighi, M. Ozbulut, A. Rahmat, J. Feng, M. Yildiz, An incompressible smoothed particle hydrodynamics method for the motion of rigid bodies in fluids, Journal of Computational Physics 297 (2015) 207–220. doi:10.1016/j.jcp.2015.05.015.

[20] A. Aly, M. Asai, Large scale simulation of fluid-structure interaction using an incompressible smoothed particle hydrodynamics, in: E. Oate, J. Oliver, A. Huerta (Eds.), 11th World Congress on Computational Mechanics, Vol. 11, International Association for Computational Mechanics, 2014.

[21] D. Price, Smoothed particle hydrodynamics and magnetohydrodynamics, Journal of Computational Physics 231 (3) (2012) 759–794. doi:10.1016/j.jcp.2010.12.011.

[22] J. Morris, P. Fox, Y. Zhu, Modeling low reynolds number incompressible flow using sph, Journal of Computational Physics 136 (1997) 214–226. doi:10.1006/jcph.1997.5776.

[23] A. Tartakovsky, P. Meakin, Modeling of surface tension and contact angles with smoothed particle hydrodynamics, Physical Review E: Statistical, Nonlinear, and Soft Matter Physics 72 (026301). doi:10.1103/PhysRevE.72.026301.

[24] R. Cole, Underwater Explosions, Princeton University Press, 1948.

[25] J. Monaghan, Simulating free surface flows with sph, Journal of Computational Physics 110 (2) (1994) 339–406.

[26] J. Hall, T. Rendall, C. Allen, H. Peel, A multi-physics computational model of fuel sloshing effects on aeroelastic behaviour, Journal of Fluids and Structures 56 (2015) 11–32.

[27] C. Fraga Filho, J. Chacaltana, Boundary treatment techniques in smoothed particle hydrodynamics: Implementations in fluid and thermal sciences and results analysis, in: Proceedings of the XXXVII Iberian Latin-American Congress on Computational Methods in Engineering, 2016.

[28] R. Dalrymple, B. Rogers, Numerical modeling of water waves with the sph method, Coastal Engineering 53 (2006) 141–147. doi:10.1016/j.coastaleng.2005.10.004.

[29] A. Crespo, M. Gomez-Gestaira, R. Dalrymple, Boundary conditions generated by dynamic particles in sph methods, Computers, Materials & Continua 5 (3) (2007) 173–184.

[30] Z. Püspöki, M. Storath, D. Sage, M. Unser, Transforms and operators for directional bioimage analysis: A survey, in: W. De Vos, S. Munck, J.-P. Timmermans (Eds.), Focus on Bio-Image Informatics, Vol. 219 of Advances in Anatomy, Embryology and Cell Biology, Springer International Publishing, 2016, Ch. 3, pp. 69–93.

[31] W. F. Lindsey, Drag of cylinders of simple shapes, Tech. Rep. 619, NACA (1938).